



Monazite trace-element and isotopic signatures of (ultra)high-pressure metamorphism: Examples from the Western Gneiss Region, Norway

Robert M. Holder ^{*}, Bradley R. Hacker, Andrew R.C. Kylander-Clark, John M. Cottle

Department of Earth Science, University of California, Santa Barbara, United States

ARTICLE INFO

Article history:

Received 11 December 2014

Received in revised form 21 April 2015

Accepted 27 April 2015

Available online 9 May 2015

Editor: Prof. K. Mezger

Keywords:

Monazite

U–Pb

Petrochronology

Trace elements

Ultrahigh pressure

Norway

ABSTRACT

Monazite U–Pb and trace-element data were gathered from six high- to ultrahigh-pressure (UHP) samples from the Western Gneiss Region, Norway, using LASS (laser-ablation split-stream ICP-MS) to investigate variations in monazite composition during high-pressure metamorphism. The UHP monazites were found to contain up to 7600 ppm Sr, 110 ppm non-radiogenic Pb, relatively weak negative Eu anomalies, and Y concentrations as low as 500 ppm. Amphibolite-facies monazite that rims the UHP monazite in one sample contains Y concentrations up to 1.6 wt.%, Sr as low as 13 ppm, and no detectable non-radiogenic Pb. The UHP monazite composition (high Sr–Pb) is interpreted to result from growth in the absence of feldspar, possibly aided by increased compatibility of Sr–Pb–Eu²⁺ in the monazite crystal structure at high pressure. Sr in monazite as a proxy for feldspar stability may be a useful tool not only in studying high-pressure metamorphism, but also in determining timescales of melting and crystallization, when the amount of feldspar changes over time.

© 2015 Elsevier B.V. All rights reserved.

1. Introduction

The development and application of in situ analytical techniques (laser-ablation ICP-MS, ion microprobe, and electron microprobe) for U/Th–Pb dating has resulted in dramatic progress in our ability to understand and unravel the complexity of mineral histories chiefly because these techniques allow us to quantify trace-element compositions and U/Th–Pb dates from the same volume of material. Attempts to tie radiometric dates to petrologic conditions (i.e., “petrochronology”) have been both quantitative and qualitative.

For monazite, quantitative approaches include monazite–quartz oxygen-isotope thermometry (Breecker and Sharp, 2007; Rubatto et al., 2014) and monazite–xenotime and monazite–garnet thermometry (Gratz and Heinrich, 1997; Heinrich et al., 1997; Pyle et al., 2001; Seydoux-Guillaume et al., 2002; McFarlane et al., 2005; Krenn and Finger, 2010). However, difficulty in assessing equilibrium (e.g., Berger et al., 2005) and poorly understood activity–composition relations due to the many end-member compositions of monazite solid solutions, often necessitate qualitative approaches. These approaches use trace-element patterns along with in situ mineral relationships (particularly inclusion relationships) to tie the time of accessory-phase (re)crystallization to the presence/absence or mode of other minerals. For monazite

dating, the most-common approach is to interpret Y and heavy rare-earth element (HREE) depletion as reflecting (re)crystallization in the presence of garnet (e.g., Zhu and O’Nions, 1999; Foster et al., 2000; Foster et al., 2002; Rubatto et al., 2013; Stearns et al., 2013). The Eu anomaly in monazite has been suggested as a qualitative monitor of rock feldspar content (Nagy et al., 2002; Rubatto et al., 2013) although this interpretation is complicated by the sensitivity of Eu²⁺/Eu³⁺ ratios to *f*_{O₂} (Wilke and Behrens, 1999; Aigner-Torres et al., 2007).

Only two studies have discussed the composition of demonstrably high-pressure monazite (Vaggelli et al., 2006; Finger and Krenn, 2007). This study aims to further understand the relationship between trace elements in monazite and the petrologic conditions at which monazite may (re)crystallize, by examining monazite from ultrahigh-pressure rocks (2.5–3.5 GPa) in the Western Gneiss region, Norway. This is an ideal place to examine the influence of high-pressure metamorphism on monazite composition, because both the timing and spatial extent of UHP metamorphism have been well documented (Fig. 1). We argue that high-Sr and common-Pb concentrations in monazite are indicative of (re)crystallization at (U)HP.

2. The Western Gneiss region, Norway

The Western Gneiss region (WGR; Fig. 1) is part of the Scandinavian Caledonides, an orogenic belt that formed from the collision of Baltica and Laurentia between 500 and 375 Ma (e.g., Corfu et al., 2014 and references therein). The terrane contains rare but widespread

^{*} Corresponding author at: 1006 Webb Hall, University of California, Santa Barbara, CA 93106, United States.

E-mail address: rholder@umail.ucsb.edu (R.M. Holder).

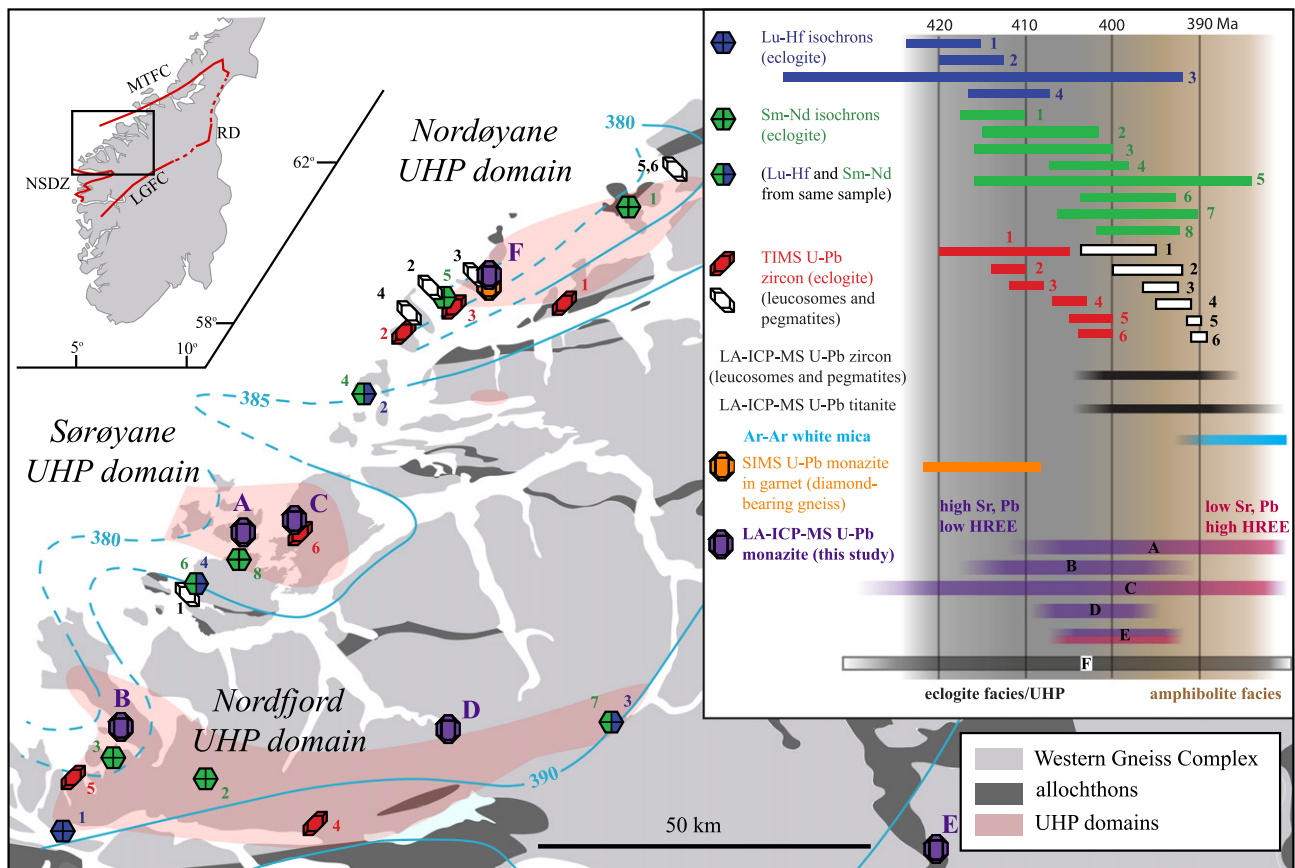


Fig. 1. Simplified geologic map and summary of geochronology used to constrain the timing of eclogite-facies/UHP metamorphism (420–400 Ma) and amphibolite-facies metamorphism (400–380 Ma). The monazites in this study with high Sr and non-radiogenic Pb have U–Pb dates compatible with UHP metamorphism. Lu–Hf isochrons are from Kylander-Clark et al. (2007, 2009). Sm–Nd isochrons from Mørk and Mearns (1986), Mearns (1986), Carswell et al. (2003b), and Kylander-Clark et al. (2007, 2009). TIMS U–Pb zircon dates from eclogites from Carswell et al. (2003a), Root et al. (2004), Young et al. (2007), and Krogh et al. (2011). TIMS U–Pb zircon dates from leucosomes and pegmatites from Krogh et al. (2011), Vrijmoed et al. (2013), and Kylander-Clark and Hacker (2014). LA–ICP–MS U–Pb zircon dates from leucosomes and pegmatites from Gordon et al. (2013) and Kylander-Clark and Hacker (2014). LA–ICP–MS U–Pb titanite dates from Spencer et al. (2013). Ar–Ar white-mica dates and contours from Root et al. (2004), Hacker et al. (2010), and Walsh et al. (2013). SIMS U–Pb monazite date from Terry et al. (2000b). Inset abbreviations: LGFC: the Lærdal–Gjende Fault Complex; MTFZ: Møre–Trøndelag Fault Complex; NSDZ: Nordfjord–Sogn Detachment Zone; RD: Røragen Detachment. Modified from Kylander-Clark and Hacker (2014).

eclogite-facies metamorphic rock and preserves three to four discrete domains that show evidence for UHP (coesite-stable) peak metamorphic conditions of 2.5–3.2 GPa and 650–800 °C (e.g., Cuthbert et al., 2000; Terry et al., 2000a; Root et al., 2004; Hacker, 2006). The onset of continental subduction in the WGR occurred around 430 Ma (e.g., Andersen et al., 1990; Kylander-Clark et al., 2009), and led to the subduction of the Baltica margin to mantle depths (Andersen et al., 1991; Hacker and Gans, 2005). The timing and duration of eclogite-facies metamorphism has been constrained to 425–400 Ma by Lu–Hf isochrons (Kylander-Clark et al., 2007; 2009) and TIMS U–Pb zircon dates from eclogites across the region (Carswell et al., 2003a; Root et al., 2004; Young et al., 2007; Krogh et al., 2011). Exhumation of the UHP rocks to mid-crustal levels occurred shortly after 400 Ma as determined by TIMS and LA–ICP–MS U–Pb zircon from discordant leucosomes and pegmatites (Krogh et al., 2011; Vrijmoed et al., 2013; Gordon et al., 2013; Kylander-Clark and Hacker, 2014), LA–ICP–MS U–Pb titanite from Western Gneiss Complex and hornblende–plagioclase leucosomes (Spencer et al., 2013), and Ar–Ar white-mica dates (Root et al., 2004; Hacker et al., 2010; Walsh et al., 2013).

3. Analytical methods

3.1. Electron-beam methods

Monazite grains were identified through back-scattered electron microscopy and energy-dispersive spectroscopy on a FEI Q400f

FEG scanning electron microscope at the University of California, Santa Barbara (UCSB). X-ray maps of the grains were produced on a Cameca SX-100 electron microprobe at UCSB. Quantitative analyses of sample A grain 1 and of all major phases in samples A and B were also conducted on the microprobe. Details of these analyses are described in Appendix 1 and the data is reported in the Supplementary material.

3.2. Pseudosection modeling

Pseudosections of samples A and B were calculated using *Perple_X* (Connolly and Pettrini, 2002) and the internally consistent thermodynamic database of Holland and Powell (2011), to assess which minerals may have been present during (U)HP monazite recrystallization. Details of this procedure are outlined in Appendix 2.

3.3. Laser-ablation split-stream (LASS) petrochronology

All grains were dated using by LASS (laser-ablation split-stream inductively coupled plasma mass spectrometry) using the *Nu Plasma HR* multi-collector and either the *Nu AttoM* high-resolution single-collector or the Agilent 7700S quadrupole ICP-MS at UCSB. Details of this method are described by Kylander-Clark et al. (2013). Specifics of the analyses in this study are described in Appendix 3 and the data are located in the Supplementary material.

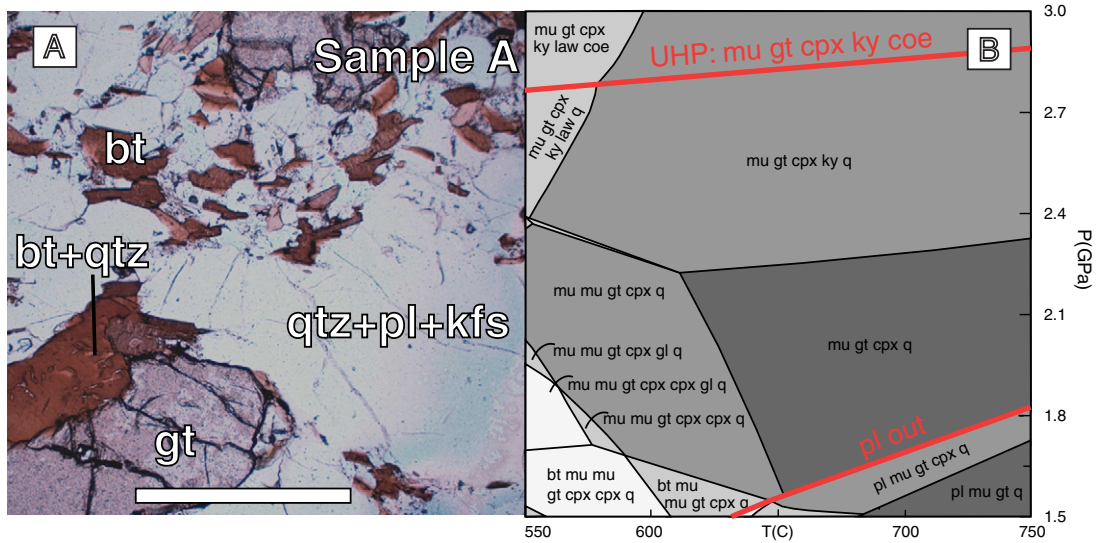


Fig. 2. A) Photomicrograph of sample A showing the low-pressure mineral assemblage observed in the rock. B) Pseudosection showing what was likely the stable mineral assemblage at UHP.

4. Samples

Six samples were studied. Two samples examined in most detail are presented in the text. The remaining 4 samples are reported in Appendix 4.

4.1. Sample A

(8828A5; Figs. 2 and 3) is a kyanite–garnet–white-mica–biotite quartzofeldspathic gneiss in the Western Gneiss Complex on Leinøya, in the center of the Sørøyane UHP domain; the gneiss outcrop contains blocks of eclogite. Major-element zoning in garnet is nearly homogeneous and shows evidence for resorption. Kyanite is also strongly resorbed. Biotite occurs in two habits: primarily tabular, large (~500 μm)

grains and fine grains (<100 μm) distributed evenly within plagioclase; the latter texture is interpreted as crystallization from a melt (Cesare, 2008). Titanite from nearby outcrops is 395–393 Ma (Spencer et al., 2013) and mica from this outcrop is 385 Ma (Walsh et al., 2013). The presence of eclogite within this outcrop and the location of this outcrop in the center of the Sørøyane UHP domain are compatible with this rock having been to UHP; the pseudosection in Fig. 2 suggests that the UHP assemblage was garnet–omphacite–phengite–kyanite–coesite.

4.2. Sample B

(8910A3; Fig. 4) is a biotite–plagioclase–quartz gneiss in the Western Gneiss complex on Stadlandet in the Nordfjord UHP domain; the gneiss outcrop contains blocks of eclogite. The rock also contains minor

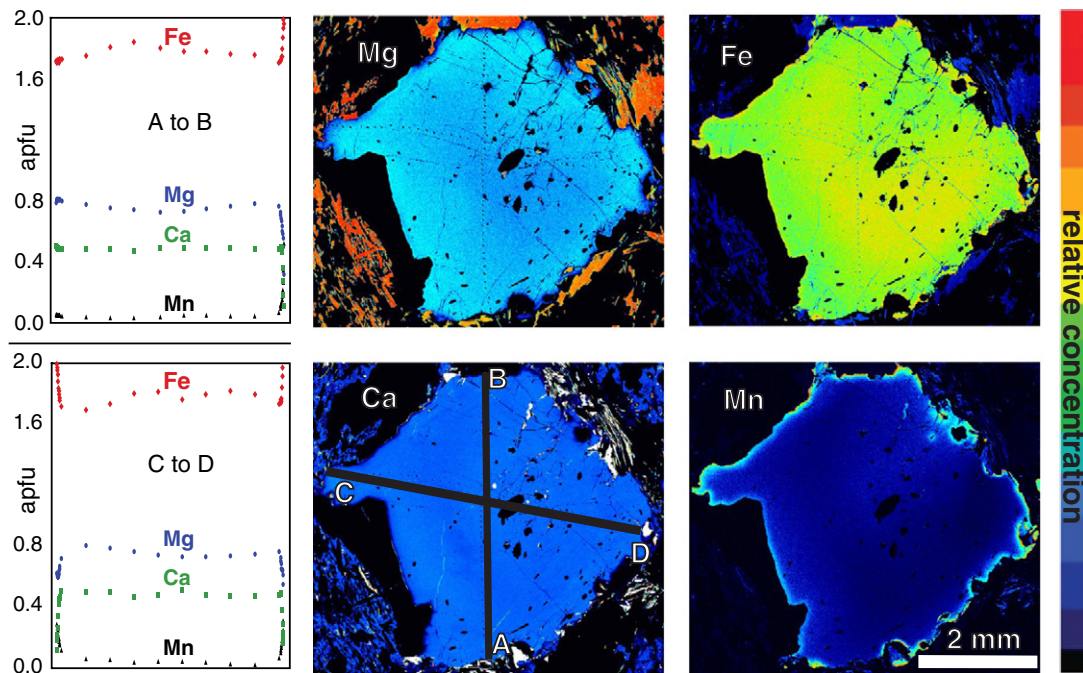


Fig. 3. Garnet X-ray maps and transects from sample A. Garnets are nearly homogeneous, with sharp variation at the rims consistent with resorption during retrogression.

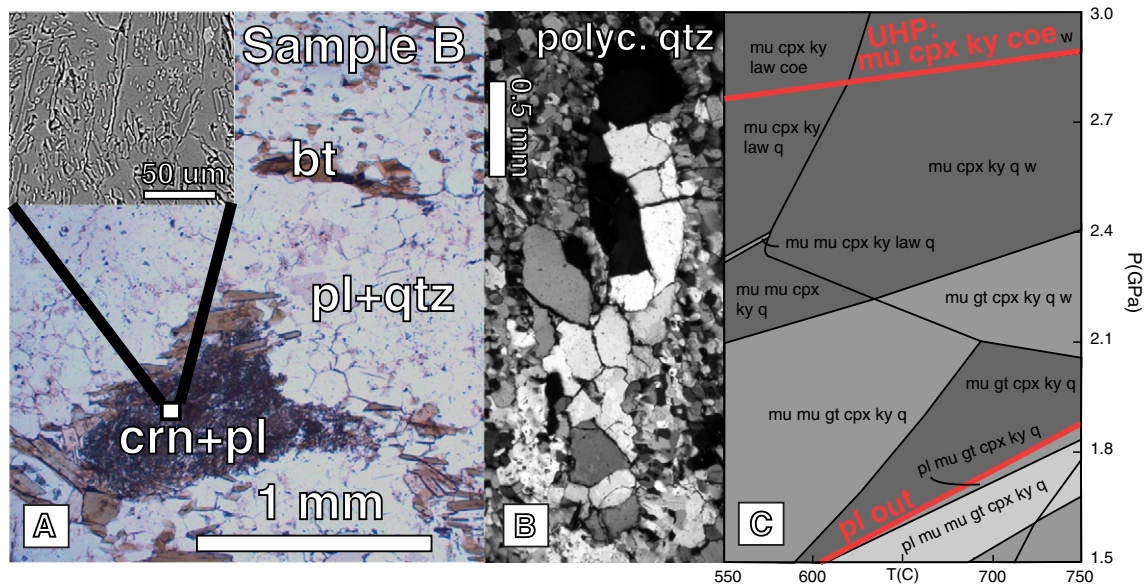


Fig. 4. A) Photomicrograph of sample B with inset back-scattered electron image showing a corundum-plagioclase symplectite. B) Cross-polarized light photomicrograph of a large polycrystalline quartz aggregate surrounded by palisade quartz, interpreted to be a pseudomorph after coesite. C) Pseudosection showing what was likely the stable mineral assemblage at UHP.

amphibole and garnet (1 grain ~100 μm , strongly resorbed). Textural and chemical disequilibrium is evident from mm-scale corundum–plagioclase symplectites and polycrystalline quartz mantled by palisade quartz. The corundum–plagioclase symplectites are likely decompression-related pseudomorphs after kyanite \pm omphacite (Möller, 1999; Nakamura and Hirajima, 2000; Baldwin et al., 2015). The presence of coesite–eclogite within a few kilometers of this outcrop, the outcrop location in the Nordfjord UHP domain, and the presence of pseudomorphs after coesite are compatible with this rock having been to UHP: the pseudosection in Fig. 4 suggests that the stable UHP assemblage was omphacite–phengite–kyanite–coesite \pm minor garnet. Titanite from granodioritic gneiss nearby is 404–393 Ma (Spencer et al., 2013) and mica from nearby is 389–374 Ma (Walsh et al., 2013).

5. Results

5.1. Intercept dates

The monazites presented here contain domains that yielded clustered, discordant U–Pb isotopic ratios. We interpret the discordance to be from non-radiogenic Pb (not inheritance from partial sampling of an older domain or Pb loss) for two reasons: the discrete groups of discordant analyses correlate with other chemical zoning (Figs. 6–9),

and there is a negative correlation between discordance and baseline-corrected $^{206}\text{Pb}/^{204}\text{Pb}$ cps (Fig. 5). In order to calculate dates for these discordant analyses, an upper intercept needs to be fixed in Tera–Wasserburg space (so-called intercept date or “ ^{207}Pb -corrected $^{206}\text{Pb}/^{238}\text{U}$ date”). To do this, we used the $^{207}\text{Pb}/^{206}\text{Pb}$ ratio of biotite in each sample as a proxy for the whole-rock Pb-isotope composition (Supplementary material). It is possible that the monazites inherited some of their common Pb from a radiogenic source, such as allanite or apatite (Romer and Siegesmund, 2003). There are no reaction textures to suggest that this happened, but if so, the calculated intercept dates would be slightly younger.

Dates in this paper are presented in the format $A \pm B$ [C]. A is the mean calculated date of a group of analyses, B is the 2σ standard error of that mean, and C is the long-term reproducibility of laser-ablation monazite dates determined empirically at the UCSB LA-ICP-MS facility (2% or ~8 Ma for 400 Ma samples; Hacker et al., 2015).

5.2. Sample A

Two monazites from this sample were examined in detail in thin section. Grain 1 (Figs. 6, 7) is a hypidioblastic, 400- μm grain adjacent to quartz, plagioclase, and biotite. X-ray maps of Y, Sr, Th, and Nd reveal four compositional domains: a sector-zoned core and two mantles with

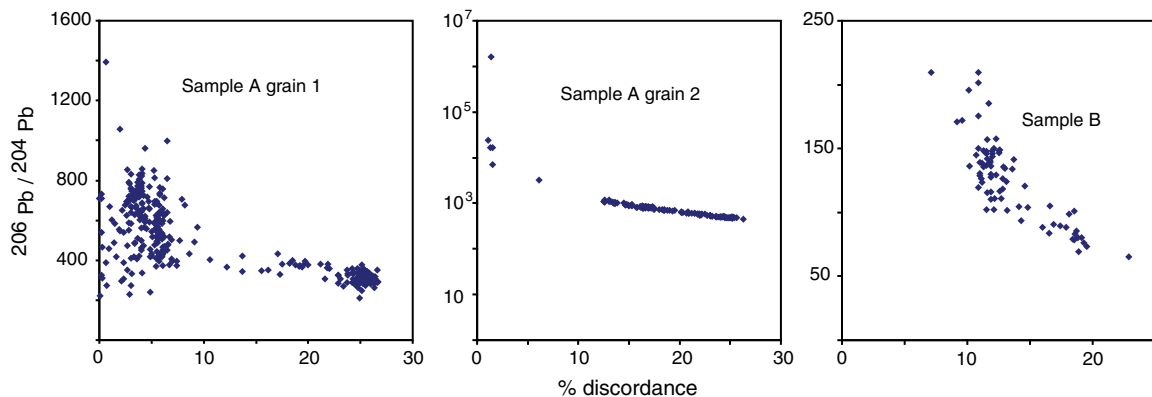


Fig. 5. Percent discordance (difference between $^{207}\text{Pb}/^{235}\text{U}$ and $^{206}\text{Pb}/^{238}\text{U}$ dates) plotted against baseline-corrected $^{206}\text{Pb}/^{204}\text{Pb}$, showing that discordance is the result of non-radiogenic Pb in the monazites.

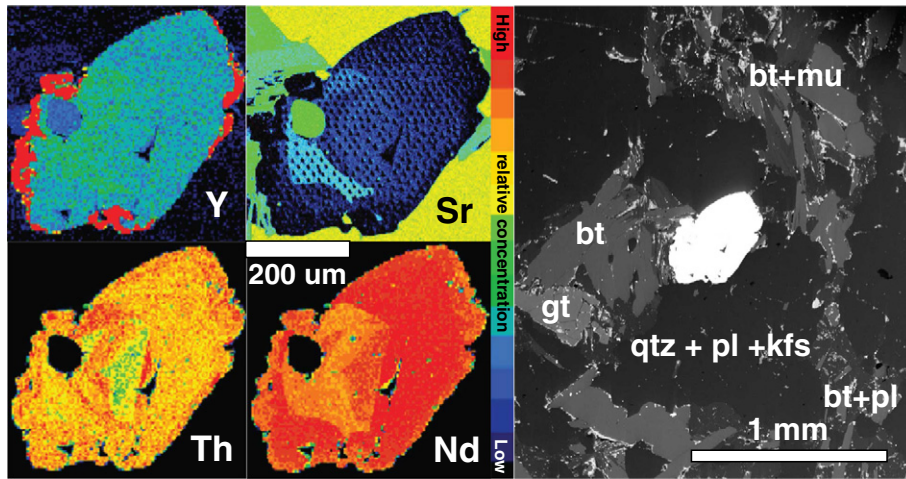


Fig. 6. X-ray maps and back-scattered electron image of monazite grain 1 in sample A.

high Sr and low Y concentrations and a rim with high Y and low Sr concentrations. U–Pb isotopes and REE were measured by LASS; Y and Sr were measured by electron microprobe. The core and mantles yielded discordant analyses, with intercept dates of 405.8 ± 3.3 [8] Ma (MSWD = 0.94, $n = 71$), 397.5 ± 2.7 [8] Ma (MSWD = 1.2, $n = 10$), and 393.4 ± 0.6 [8] Ma (MSWD = 0.82, $n = 71$). The rim yielded concordant to near-concordant isotopic ratios with a mean $^{206}\text{Pb}/^{238}\text{U}$ date of 387.2 ± 1.4 [8] Ma (MSWD = 1.8, $n = 17$). The core contains 0.16 to 0.24 wt.% Sr, 0.70 to 0.90 wt.% Y, and 23 to 107 ppm non-radiogenic Pb. The inner mantle contains 0.49 to 0.53 wt.% Sr, 0.80 to 1.0 wt.% Y, and 19 to 46 ppm non-radiogenic Pb. The outer mantle contains 0.04 to 0.18 wt.% Sr, 0.05 to 0.46 wt.% Y, and 1 to 15 ppm non-radiogenic Pb. The rim contains 13,600 to 16,000 ppm Y and 0 to 3 ppm non-radiogenic Pb; Sr is below the EPMA detection limit (50 ppm).

Grain 2 (Figs. 8, 9) is a xenoblastic, 300- μm grain surrounded by biotite. X-ray maps of Y, Sr, Th, U, and Pr show two main compositional zones in the grain: a core with high Sr and low Y concentrations and a rim with high Y and low Sr concentrations. All quantitative analyses were done by LASS. The core of the grain yielded discordant analyses with an intercept of 391.0 ± 0.8 [8] Ma (MSWD = 2.0, $n = 120$). The rim analyses are nearly concordant, with an intercept of 377.5 ± 6.1 [8] Ma (MSWD = 6.5, $n = 6$). The core has 1900 to 4000 ppm Sr, 600 to 850 ppm Eu, 700 to 7000 ppm Y, and 4 to 43 ppm non-radiogenic Pb; in contrast to the rim which has 13 to 80 ppm Sr, 550 to 640 ppm Eu, 7500 to 14,000 ppm Y, and 1 to 4 ppm non-radiogenic Pb.

5.3. Sample B

One hypidioblastic, 300- μm grain adjacent to plagioclase and biotite in thin section was examined (Figs. 10, 11). X-ray maps of Th, Y, U, and Pr show an embayed core, a mantle, and four <20- μm Y-rich domains that appear to be compositionally related to a thin discontinuous rim (<5 μm). The thin section peeled off of its glass slide before X-ray maps of Sr zoning could be made. All quantitative analyses were done by LASS. The core of the grain yielded an intercept date of 410.7 ± 1.7 [8] Ma (MSWD = 0.9, $n = 16$). The mantle of the grain gave an intercept date of 398.0 ± 1.1 [8] Ma (MSWD = 1.5, $n = 62$). One analysis partially sampled one of the small, Y-rich domains in the interior of the grain, but its U–Pb isotopic ratios are indistinguishable from the mantle. The core has 4200 to 7600 ppm Sr, 1300 to 2600 ppm Y, 830 to 1300 ppm Eu, and 24 to 41 ppm non-radiogenic Pb. The mantle has 2500 to 5500 ppm Sr, 1700 to 3700 ppm Y, 800 to 1400 ppm Eu, and 7 to 22 ppm non-radiogenic Pb. The small Y-rich domain that was partially sampled contained 9300 ppm Y. The rim was too thin to analyze.

6. Discussion

6.1. Relationship between monazite dates and UHP metamorphism

The monazite dates from sample A can be tied to UHP with both the trace-element compositions and the U–Pb dates. Low-Y–HREE

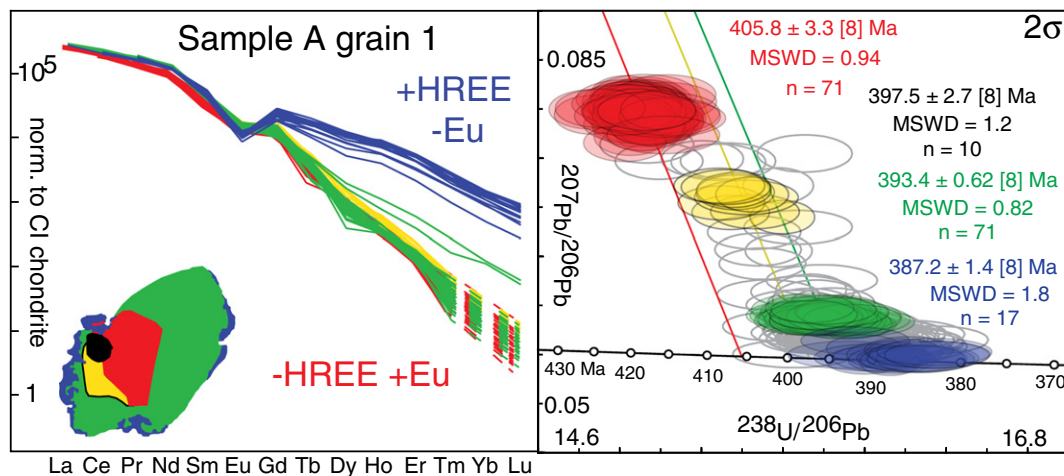


Fig. 7. U–Pb concordia diagram and REE plot from LASS analyses of grain 1 in sample A. The UHP core and mantles of the grain contain lower HREE concentrations, weaker negative Eu anomalies, more common Pb, and higher Sr concentrations than the low-pressure rim. See Supplementary material for monazite Sr microprobe analyses.

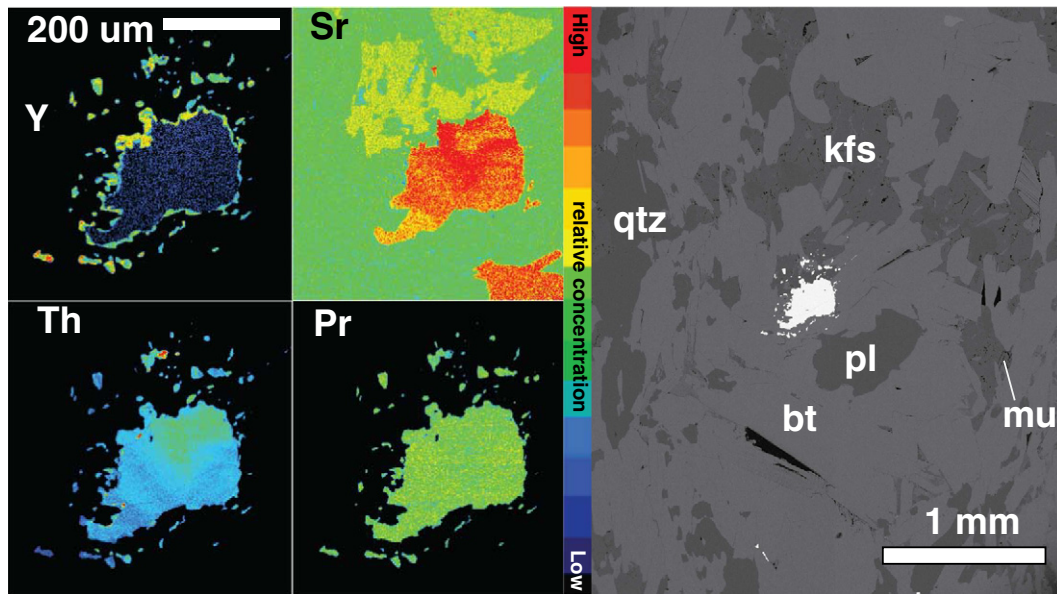


Fig. 8. X-ray maps and back-scattered electron image of monazite grain 2 in sample A.

monazite cores are interpreted as having (re)crystallized in the presence of garnet, a stable UHP phase in this rock (Fig. 2). Likewise, the high-Y–HREE rims of the grains are compatible with monazite (re)crystallization during or after garnet breakdown (lower-P). In addition, the intercept dates of the cores coincide with the established timing of UHP metamorphism (Fig. 1), whereas the dates from the rims are distinctly post-UHP.

Unlike sample A, the monazite from sample B has little trace-element variation except for a few small domains with high Y. This may be because this rock did not have garnet at peak-pressure (Fig. 4) or because the amount of garnet was small (<1.5 modal % is predicted over the PT range modeled). The most-reliable indication that the monazite from sample B (re)crystallized at UHP is that the dates coincide with the timing of UHP as determined by dating of eclogites within the UHP domain nearby (Lu–Hf isochrons, and TIMS U–Pb zircon; Fig. 1).

6.2. Sr, Eu, and common Pb in monazite

High-Sr, low-Y monazites have been found in both the Bohemian Massif (Finger and Krenn, 2007) and in the Dora Maira Massif (Vaggelli et al., 2006), both of which experienced UHPM. The high-Sr

monazites from Dora Maira (1000–3000 ppm Sr) are inclusions in pyrope megablasts from whiteschists within the Brossasco–Isasca Unit. The high-Sr monazites from the Bohemian Massif (1.7 wt.% Sr) are inclusions in garnet in a >60% garnet rock from the Podolsko Complex. The authors interpreted the elevated Sr to be a result of high-pressure plagioclase breakdown that released Sr.

At normal crustal pressures, larger negative Eu anomalies in monazite have been related to the growth of feldspar from melt (Nagy et al., 2002; Rubatto et al., 2013). However, this interpretation is complicated by the sensitivity of $\text{Eu}^{2+}/\text{Eu}^{3+}$ ratios to f_{O_2} (Wilke and Behrens, 1999; Aigner-Torres et al., 2007), which may not be constant, especially in magmatic environments.

It is commonly assumed that monazite does not incorporate significant Pb during crystallization (e.g., Parrish, 1990; Suzuki and Adachi, 1991). Although many monazite dates are concordant or near-concordant, monazites routinely yield at least some, and occasionally only, discordant data. This is especially pronounced in Cenozoic rocks in which little radiogenic Pb has accumulated (e.g., the hydrothermal monazites of Janots et al., 2012; the metamorphic monazites of Mottram et al., 2014), but some older monazites also show isotopic ratios that are dispersed from concordia toward common-Pb (e.g.,

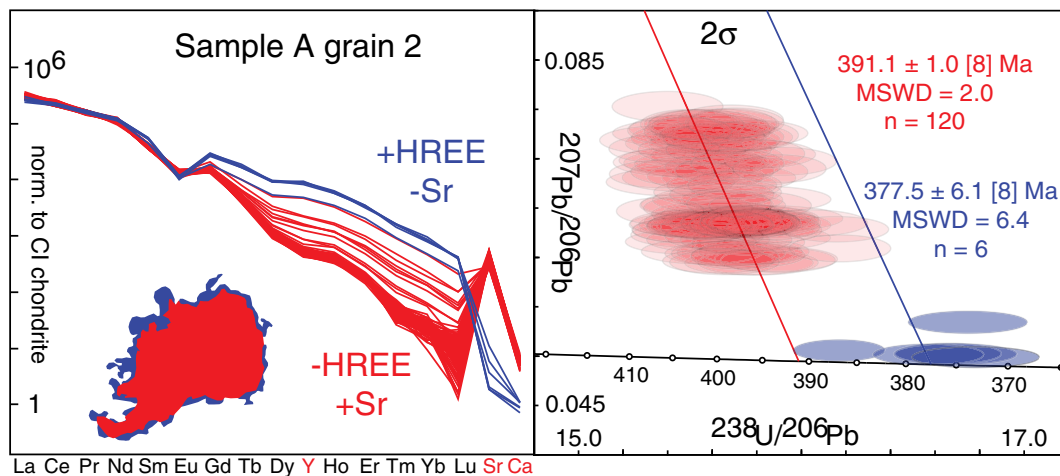


Fig. 9. U–Pb concordia diagram and REE plot from LASS analyses of grain 2 in sample A. Y, Sr, and Ca have been added to the typical REE diagram in order to display them alongside the REE for easy comparison. The UHP core of the grain contains lower HREE concentrations, weaker negative Eu anomalies, more common Pb, and higher Sr concentrations than the low-pressure rim.

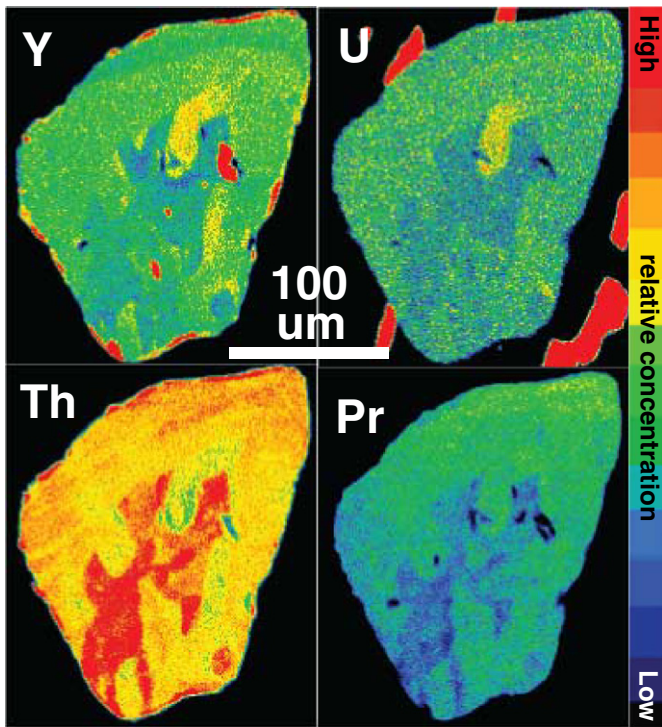


Fig. 10. X-ray maps of the large monazite investigated from sample B.

Broussole et al., 2015). Furthermore, monazites that were originally concordant can become discordant by alteration in the presence of low-temperature hydrothermal fluids (<400 C; Poitrasson et al., 2000; Seydoux-Guillaume et al., 2012). A key difference between this study and the studies mentioned above is that the non-radiogenic Pb in the monazites of this study is concentrated in specific zones with distinct trace-element characteristics.

High Sr–Eu–Pb in the high-pressure monazites from this study could be the result of two different mechanisms: 1) increased partitioning of Sr–Eu²⁺–Pb into monazite due to a phase change, such as the loss of feldspar (Finger and Krenn, 2007) or another phase that partitions Sr–Eu²⁺–Pb strongly (Ewart and Griffin, 1994; Bindeman et al., 1998; Spandler et al., 2003; Aigner-Torres et al., 2007) or 2) increased compatibility of Sr–Eu²⁺–Pb in the monazite crystal structure at high pressure regardless of the stability of other minerals.

In sample A, the Sr concentrations vary by more than two orders of magnitude (13 to 5300 ppm), suggesting that a change in compatibility is unlikely to be the only cause of the compositional range observed. The most-important phase changes observed in the modeling of samples A and B are the breakdown of feldspar and biotite and the growth of clinopyroxene and (additional) white-mica (Figs. 2, 4). Biotite and white-mica have a similar crystal structure, so the loss of feldspar probably has a larger effect on the Sr–Eu²⁺–Pb budget of the rock. We therefore interpret the high Sr–Eu²⁺–Pb monazites to reflect (re)crystallization in the absence of feldspar, although increased compatibility of Sr–Eu²⁺–Pb in monazite at UHP may also play a role.

7. Conclusions

Proximity to eclogites in the field, measured U–Pb dates, and HREE compositions indicate monazite recrystallization at UHP. These UHP monazites are characterized by high Sr (thousands of ppm) and non-radiogenic Pb (up to 100 ppm) as well as weaker negative Eu anomalies. Elevated Sr–Eu²⁺–Pb in the UHP monazites may be the result of the feldspar instability at pressures above 1.5 GPa and/or increased compatibility of Sr–Eu²⁺–Pb into monazite. If Sr in monazite is controlled primarily by the stability of feldspar, it should provide a useful tool not only in identifying the timing of high-pressure metamorphism, but also in determining timescales of melting and crystallization in high-temperature metamorphic environments.

Acknowledgments

Frank Spera and an anonymous reviewer provided invaluable feedback on trace-element partitioning among phases. Gareth Seward conducted the electron microprobe Sr analyses and maps. Demian Nelson provided standard glass analyses that allowed quantification of Sr in the monazite RMs. Sophie Briggs, Tyson McKinney, and Josh Garber provided many informal discussions of monazite dating and chemistry. Funded by NSF EAR-1050043 to Cottle, NSF EAR-1219942 and NSF-EAR-0911485 to Hacker, and the University of California, Santa Barbara.

Appendix 1. Characterization of monazites by electron microprobe

Monazite grains were identified through back-scattered electron microscopy and energy-dispersive spectroscopy on a FEI Q400f FEG scanning electron microscope at the University of California, Santa Barbara (UCSB). Different chemical domains in monazite were characterized with X-ray maps of Y, La, Nd, Pr, Th, U and Sr created using a Cameca SX-100 electron microprobe at UCSB. The maps were

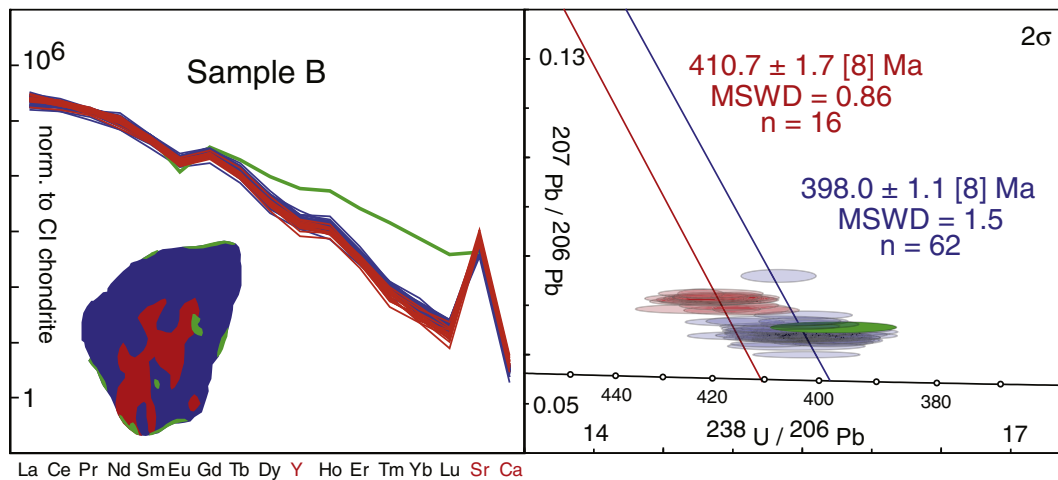


Fig. 11. U–Pb concordia diagram and REE plot from LASS analyses of the large monazite investigated in sample B. Y, Sr, and Ca have been added to the typical REE diagram for easy comparison. All analyses are interpreted to be UHP. They have high Sr concentrations and moderate HREE concentrations except for one analysis with higher HREE.

constructed using an accelerating voltage of 15 keV, a 200 nA beam current, a 0.5–1 $\mu\text{m}/\text{pixel}$ step size, and a dwell time of 0.2 s.

Quantitative compositional analyses of 1 monazite grain in Sample A were conducted on the Cameca SX-100 electron microprobe at UCSB using an accelerating voltage of 15 keV, current of 200 nA, on-peak count-times of 20 s, and off-peak count-times of 10 s on both sides of the peaks. The elements, X-ray lines, and standards measured are shown in the Supplementary material. Monazite X-ray spectra are notorious for having many interfering elements and so it is essential to demonstrate that the Sr measured in sample A is actually Sr and not an interference. To check this, a wavescan was taken across the Sr peak on the unknown (Fig. A.1). The largest potential interference is from La $L\beta_2$ (iii order) which has a 21.4% interference with the measured Sr $L\alpha$ (if there were 1 wt.% elemental Sr and 99 wt.% elemental La, the measured Sr would be 1.214 wt.%, 21.4% higher than the real amount). Based on the measured La concentrations (11.3–13.5 wt.%), the Sr measurements are at most 0.026 wt.% over estimated from this interference. There are also two Dy interferences: Dy $L\beta_1$ (iv order) at 1305% and Dy $L\beta_4$ (iv order) at 212%, but Dy concentrations are ubiquitously low or below detection limit (0.01–0.02 wt.%) in the analyses with high Sr and the analyses with higher Dy (0.34–0.44 wt.%) have Sr concentrations below the detection limit, so these interferences are not likely to have influenced the Sr measurements.

Appendix 2. Pseudosections

To evaluate what the equilibrium assemblages at UHP might have been in samples A and B, pseudosections were calculated with *Perple_X* (Connolly and Pettrini, 2002) using the internally consistent thermodynamic database of Holland and Powell (2011). Both of these samples contain definitive disequilibrium textures (resorbed grains, evidence for melt, symplectites, and pseudomorphs) and so the purpose of these pseudosections is not to determine a detailed PT history, but rather to estimate the peak-pressure equilibrium mineral assemblage with which the monazites might have crystallized. The bulk-rock compositions were determined using microprobe analyses of major phases (garnet, biotite, and plagioclase; Supplementary material) whose modes were estimated with *ImageJ*. The analyses were conducted with a 200 nA beam current, an accelerating voltage of 15 keV, 30 s on-peak count time, and a mean-atomic-number background correction. The bulk-rock compositions used in the pseudosections are shown in the Supplementary material. Sample A was modeled with H_2O saturation, whereas sample B was modeled using 1.2 mol% H_2O (estimated from the modal abundance of biotite), because the stability of

garnet in this rock is sensitive to H_2O abundance. The stability of garnet was also sensitive to FeO content; for example a change from 0.40 to 0.45 mol% FeO results in a ~ 0.5 GPa increase in the P stability of garnet.

Appendix 3. Laser-ablation split-stream (LASS) petrochronology

All grains were dated using the LASS (laser-ablation split-stream inductively coupled plasma mass spectrometry) facility at UCSB. The facility consists of a Photon Machines 193 nm excimer laser with a *HelEx* sample cell coupled to two mass spectrometers—a Nu *Plasma HR* multi-collector ICP-MS and either a Nu *AttoM* high-resolution single-collector ICP-MS or an Agilent 7700S quadrupole ICP-MS—allowing simultaneous chronology and trace-element measurements (Kylander-Clark et al., 2013). U, Th, and Pb isotopes were measured on the *Plasma HR*, however only U–Pb dates are shown in the paper, because the $^{232}\text{Th}/^{208}\text{Pb}$ value of monazite reference material 44069 has not been measured by isotope dilution. In samples A grain 1, C, D, E and F1, the lanthanides were measured on the *AttoM*. In samples A grain 2, B and F2, the lanthanides + Ca + Sr + Y were measured on the 7700S. The analyses were obtained with a 7 or 10 μm laser spot, using a frequency of 3 Hz, a 20 s ablation time, and an ablation rate of ~ 100 nm/pulse. The final pit depths were ~ 6 μm .

All data were processed using *Iolite* version 2.3 (Paton et al., 2011), which corrects for down-hole fractionation and machine drift using a matrix-matched primary reference material (RM) interleaved with the unknowns. The primary RM was 44069 monazite (Aleinikoff et al., 2006) for U–Pb ratios, and Bananeira monazite (Kylander-Clark et al., 2013; Palin et al., 2013) for trace elements. Bananeira monazite was used as a secondary RM for U–Pb ratios to assess accuracy of the unknown analyses, and additional uncertainty was added, in quadrature, to each analysis to account for variation in secondary-RM isotopic ratios within runs. The long-term reproducibility of secondary RMs indicate that monazite U–Pb dates in the UCSB LA-ICP-MS laboratory have a total uncertainty of $\sim 2\%$ (Hacker et al., 2015) that must be used when considering the absolute ages of the monazites reported herein. Data were not corrected for common Pb, because the $^{204}\text{Pb} + \text{Hg}$ signal for the RMs was indistinguishable from background (although the $^{204}\text{Pb} + \text{Hg}$ signal is distinguishable from background in unknown analyses. See Fig. 5).

U–Pb data were evaluated using *Isoplot* (Ludwig, 2008). Trace elements were normalized to McDonough and Sun (1995) CI carbonaceous chondrite values. HREE profiles become noisy as HREE concentrations decrease, due to higher uncertainty and potentially from MREE-oxide interferences. Although this influences the accuracy of the HREE profiles at ppm-level concentrations, it does not influence our interpretations, which are based on qualitative trace-element enrichment/depletion.

Sr determination in monazite RMs

The elemental Sr concentrations in monazite RMs 44069 and Bananeira are too low to be measured accurately and precisely by electron microprobe and were estimated from ICP-MS analyses. LA-ICP-MS analyses of the standard glasses NIST SRM 612 (Pearce et al., 1997; Jochum et al., 2011) and MPI-DING StHs6/80-G, ML3B-G, and ATHO-G (Jochum et al., 2006) show that Sr cps/ppm vs. Ca cps/ppm define a linear trend that projects through zero: Sr cps/ppm = $1.63 \times \text{Ca cps/ppm}$ (Supplementary material). When applied to the monazite RMs 44069 and Bananeira, for which the concentrations of Ca are known, this relationship returns Sr concentrations of 28 ± 5 ppm for 44069 ($n = 20$, MSWD = 10.3) and 0.6 ± 0.1 ppm for Bananeira ($n = 20$, MSWD = 1.7) (uncertainties only include the mean cps of the reference material analyses). The MSWDs indicate that Bananeira has a more-homogeneous Sr concentration than 44069, as is the case with REE (Kylander-Clark et al., 2013). Because of the way that these values

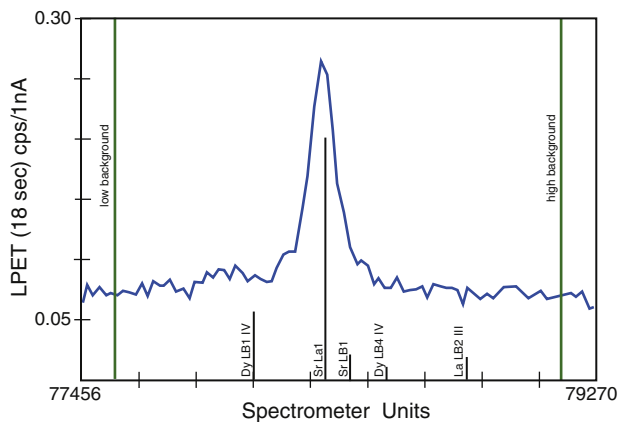


Fig. A.1. Wavelength spectrum from sample A grain 1 across the Sr $L\alpha$ peak showing the positions and relative magnitudes of potential interferences in monazite. The Sr $L\alpha$ line defines an easily recognizable, discrete peak in monazites with high enough Sr concentrations.

were calculated, the Sr concentrations in the unknowns are semi-quantitative.

Appendix 4. Additional samples

Four additional samples were found to show similar U–Pb isotope patterns to the samples discussed in the main text. Photomicrographs of these additional samples are given in Fig. D.1. U–Pb and REE data are shown in Figs. D.2 and D.3.

Sample C

(R9823A2): This rock is a kyanite–sillimanite–garnet quartzofeldspathic mylonite in the Blåhø nappe adjacent to the Hareidlandet–Dimnøya eclogite (Mysen and Heier, 1971). Garnet is strongly resorbed, and contains rutile + quartz inclusions. Kyanite is deformed, resorbed, and overgrown by oriented and unoriented sillimanite. Fine-grained biotite + plagioclase intergrowths were derived from either high-pressure mineral decomposition or melting (Cesare, 2008); these are strongly deformed.

Sample D

(P5624E): This rock is a garnet–biotite–muscovite–kyanite–sillimanite quartzofeldspathic gneiss in the Western Gneiss complex on Austefjord; the gneiss outcrop contains blocks of eclogite. Quartz shows undulatory extinction and subgrain development. Garnets are resorbed and broken. Biotite occurs in three habits: i) coarse and parallel to the foliation, ii) concordant and discordant to the foliation and intergrown with sillimanite and iii) very fine grained and intergrown with very fine-grained quartz and/or feldspar; the discordant grains with sillimanite are interpreted to reflect mica dehydration melting, and the very fine intergrowth with biotite is interpreted to reflect crystallization of a melt (Cesare, 2008). Resorbed kyanite is also present. We interpret the assemblage in this rock as representing post-UHP amphibolite-facies equilibration, melting, and deformation.

Sample E

(E9817G8): This rock is a kyanite–garnet–staurolite–biotite gneiss in the Blåhø nappe near Grotli (~50 km from the nearest coesite eclogite); the gneiss outcrop contains blocks of eclogite. Staurolite is euhedral. Garnet is euhedral–subhedral and resorbed with rutile inclusions; other minerals are coarse. Minor sillimanite is present along biotite grain boundaries. Minor chlorite is present in porphyroblast strain shadows. Pressures and temperatures of 1.15 GPa and 650 °C were determined for this outcrop using garnet–biotite and garnet–kyanite–quartz–plagioclase equilibria (Walsh and Hacker, 2004). These PT conditions were interpreted to be part of a regional post-UHP “supra-Barrovian” metamorphic event, associated with stalling of the WGR at lower-crustal depths during exhumation. Titanite from this region is Precambrian (Tucker et al., 1990) and muscovite from this outcrop is 393 Ma (Walsh et al., 2013).

Sample F

(H3630B): This rock is a diamond-bearing kyanite–garnet–biotite gneiss on Fjørtoft (Dobrzhinetskaya et al., 1995); it has been interpreted as part of the Blåhø nappe by Terry et al. (2000a). In thin section, the gneiss is composed of slightly resorbed garnets and bent kyanite in a matrix of fine-grained feldspar, quartz, and biotite.

5. Results

Sample C

The analyses for sample C come from ten different matrix grains in thin section. The grains have low-Y cores and rims of high-Y embayments and fingers (Fig. D.2). The cores yielded discordant analyses with an intercept date of 394.8 ± 1.2 [8] Ma (MSWD = 1.3, n = 22) and low HREE concentrations, whereas the rims have a mean $^{206}\text{Pb}/^{238}\text{U}$ age of 390.0 ± 2.1 [8] Ma (MSWD = 2.5, n = 22) with elevated HREE concentrations. Eu concentrations show no relationship to U–Pb date (7–1060 ppm in the rims vs 560–1150 in the cores). An additional six discordant analyses from the cores are as old as 426.9 ± 5.6

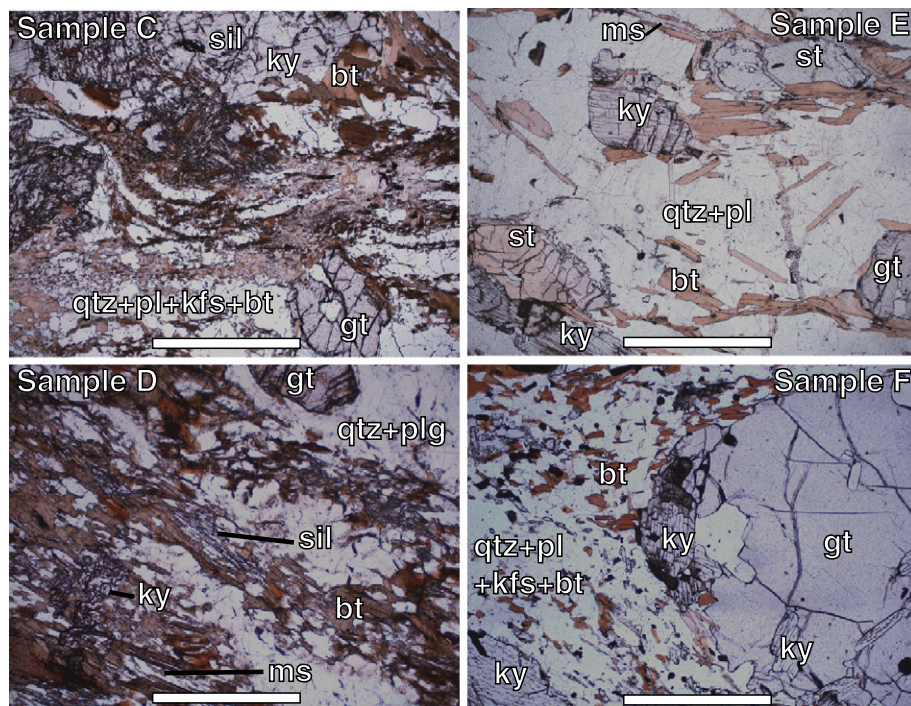


Fig. D.1. Photomicrographs of samples C through F. Scale bars are 1 mm.

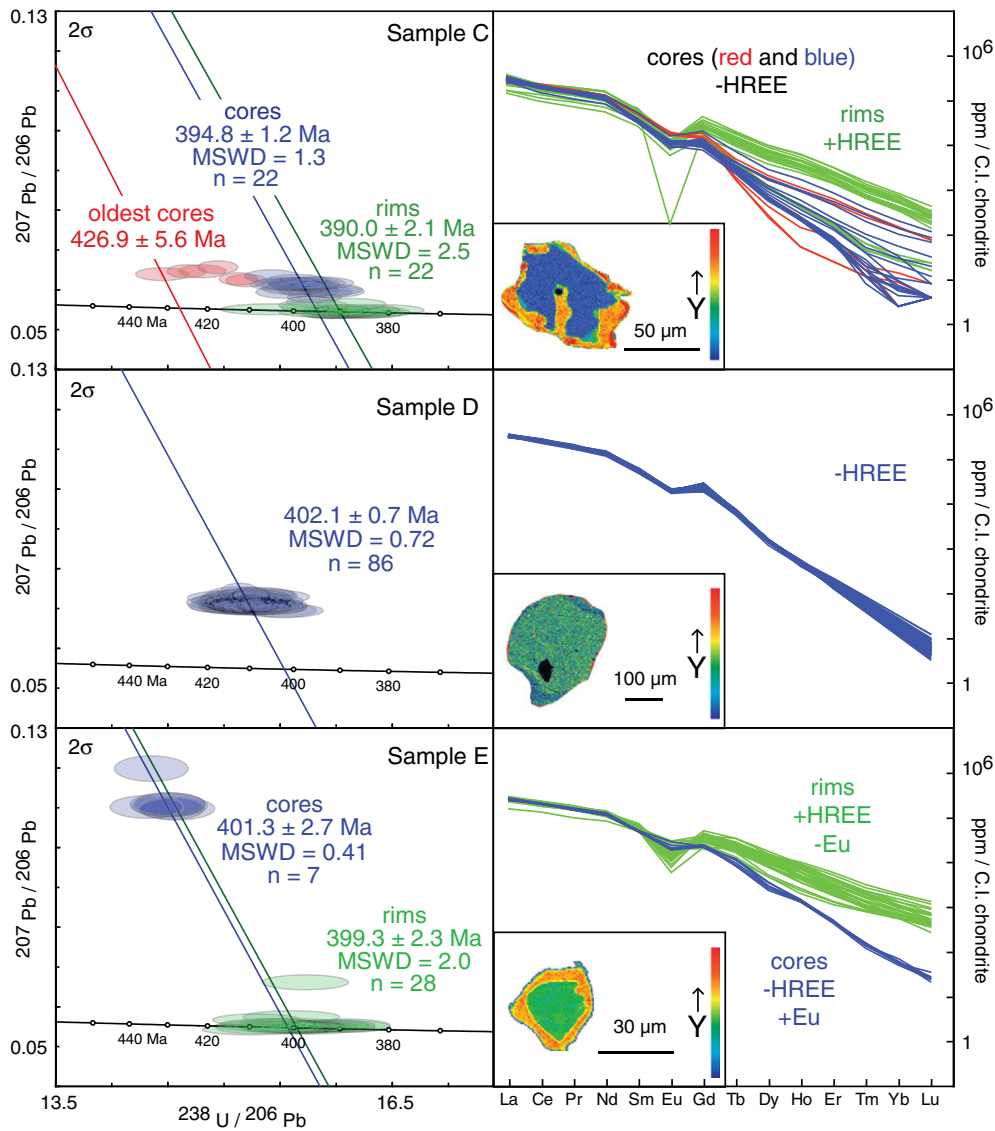


Fig. D.2. U–Pb and REE data of samples C, D, and E. All samples show discordant data, clustered around the same U–Pb isotope values, with depleted HREE concentrations. As with samples A and B, these data are interpreted to result from UHP recrystallization, although Sr was not measured. The concordant rim analyses with high HREE concentrations are interpreted as amphibolite-facies growth.

[8] Ma and have the same REE patterns as the rest of the cores. The concordant analyses have 0 to 2 ppm non-radiogenic Pb, whereas the discordant analyses have 4 to 12 ppm non-radiogenic Pb.

Sample D

Data from sample D come from 13 grains in thin section with homogenous, low-Y cores and thin (<5 μm) Y-rich rims. The rims were not analyzed. The data from the cores form a single population of discordant analyses with depleted HREE profiles, 16 to 39 ppm non-radiogenic Pb, and an intercept date of 402.1 ± 0.7 [8] Ma (MSWD = 0.7 n = 86) (Fig. D.2).

Sample E

Six monazites in thin section from sample E are characterized by low-Y cores and high-Y rims. The data form a population of discordant analyses with an intercept of 401.3 ± 2.7 [8] (MSWD = 0.4, n = 7) and a cluster of concordant to near-concordant analyses with a mean $^{206}\text{Pb}/^{238}\text{U}$ date of 399.3 ± 2.3 [8] Ma (MSWD = 2.0, n = 28) (Fig. D.2). The discordant analyses have 1100 to 1600 ppm Eu, depleted HREE profiles, and 62 to 74 ppm non-radiogenic Pb. The concordant to

near-concordant analyses have 340 to 1700 ppm Eu, elevated HREE profiles, and 0 to 11 ppm non-radiogenic Pb.

Sample F

>100 monazite grains in three thin sections were analyzed from sample F. The monazite grains are <50 μm (often <30 μm), xenoblastic, and commonly have Y-rich cores surrounded by Y-poor mantles. The first thin section (F1) is typical of the outcrop, containing only garnets <1 cm in diameter. The U–Pb dates can be divided into two broad groups: Caledonian (dates from 430 to 390 Ma) and mixing between Caledonian and Precambrian (1200–900 Ma) (Fig. D.3). The Precambrian dates correspond to the Y-rich cores of the grains and are not discussed further. The Caledonian dates can be divided into three groups based on chemistry and U–Pb date: 9 analyses with enriched HREE profiles from monazites included in garnet yielded a date of 425.5 ± 3.0 [8] Ma (MSWD = 2.3); 13 monazite analyses from grains in the matrix with depleted HREE yielded a date of 426.8 ± 1.7 [8] Ma (MSWD = 0.93); and 23 analyses from grains in the matrix with depleted HREE yielded a mean intercept of 393.0 ± 3.0 [8] Ma, but considerable scatter in U–Pb ratios (MSWD = 7.7). The other two thin sections (F2) define a transect across a 10 cm garnet. No relationship between

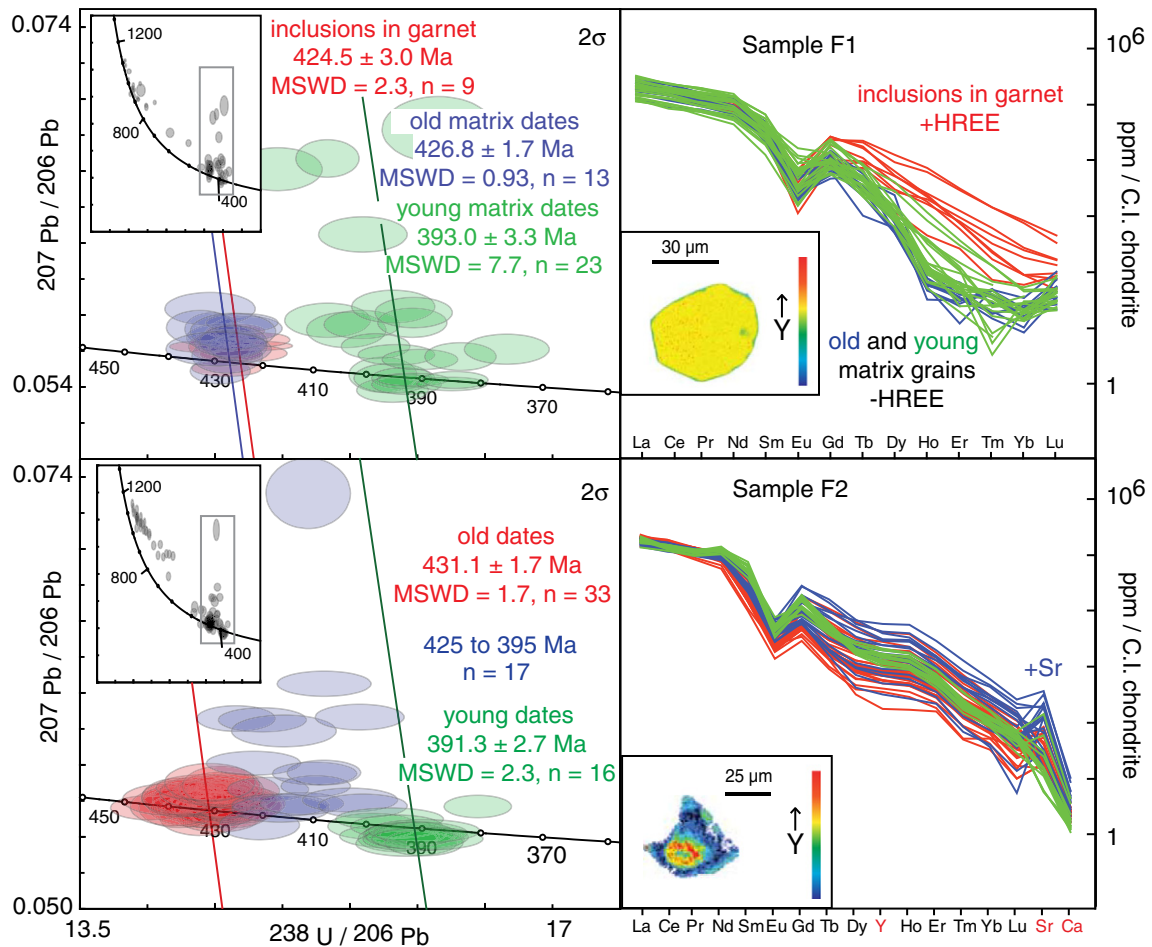


Fig. D.3. U–Pb and trace-element data for samples F1 and F2. Both samples show discordant analyses with intercept dates compatible with the timing of UHP metamorphism, but the scatter in the data makes them difficult to interpret.

the positions of the monazites within the garnet and U–Pb date or trace-element compositions was found. The Caledonian dates can be divided into three groups: concordant to near-concordant analyses at 431.1 ± 1.7 [8] Ma (MSWD = 1.7, $n = 33$ ta); analyses between 425 and 395 Ma with variable discordance; and concordant to near-concordant analyses at 391.3 ± 2.7 [8] Ma (MSWD = 2.3, $n = 16$). The REE concentrations are highly variable but have no objective relationship to U–Pb date. Non-radiogenic Pb is <10 ppm and Sr is <570 ppm in all analyses except for 7 discordant analyses between 425 and 395 Ma that have 750 to 1600 ppm Sr and 10 to 37 ppm non-radiogenic Pb.

Relationship between monazite dates from samples C–F and (U)HP metamorphism

The monazite dates from samples C, D, E can be tied to eclogite-facies metamorphism with both the trace-element compositions and the U–Pb dates. Low-Y–HREE monazite cores are interpreted as having (re-)crystallized in the presence of garnet, which all samples contain and was presumably stable at peak pressures. Likewise, the high-Y–HREE rims of the grains are compatible with monazite (re)crystallization during or after garnet breakdown (lower P). In addition, the intercept dates of the cores coincide with the established timing of UHP metamorphism (Fig. 1), whereas the dates from the rims are more likely post-UHP.

Sample F contains monazite dates that span the duration of high-pressure metamorphism. Sample F1 shows a clear transition from HREE-enriched monazite included in garnet to HREE-depleted monazite located in the matrix at 425 Ma, compatible with garnet growth at that time. This is consistent with the timing of prograde

metamorphism in the region (Fig. 1). Sample F2 gave several discordant analyses with higher Sr concentrations and intercept ages consistent with the timing of UHP; however, because all of these analyses come from monazites included within a single 10 cm garnet, the extent with which monazite could equilibrate with the rest of the rock during re-crystallization is unknown, making interpretation of the trace-element signatures difficult. Both samples F1 and F2 have dates compatible with the timing of exhumation and amphibolite-facies metamorphism, but none of these analyses show the enrichment in HREE expected from the breakdown of garnet during this process.

Appendix 5. Supplementary data

Supplementary data to this article can be found online at <http://dx.doi.org/10.1016/j.chemgeo.2015.04.021>.

References

- Aigner-Torres, M., Blundy, J., Ulmer, P., Pettke, T., 2007. Laser-ablation ICPMS study of trace element partitioning between plagioclase and basaltic melts: an experimental approach. *Contrib. Mineral. Petrol.* 153, 647–667.
- Aleinikoff, J.N., Schenck, W.S., Plank, M.O., Srogi, L., Fanning, C.M., Kamo, S.L., Bosbyshell, H., 2006. Deciphering igneous and metamorphic events in high-grade rocks of the Wilmington Complex, Delaware: morphology, cathodoluminescence and backscattered electron zoning, and SHRIMP U–Pb geochronology of zircon and monazite. *GSA Bull.* 118 (1–2), 39–64.
- Andersen, T.B., Skjerlie, K.P., Furnes, H., 1990. The Sunnfjord mélange, evidence of Silurian ophiolite accretion in the West Norwegian Caledonides. *J. Geol. Soc. Lond.* 147, 59–68.
- Andersen, T.B., Jamtveit, B., Dewey, J.F., Swenson, E., 1991. Subduction and eduction of continental crust: major mechanisms during continent–continent collision and

- orogenic extensional collapse, a model based on the south Norwegian Caledonides. *Terra Nova* 3, 303–310. <http://dx.doi.org/10.1111/j.1365-3121.1991.tb00148.x>.
- Baldwin, J.A., Powell, R., White, R.W., Stipska, P., 2015. Using calculated chemical potential relationships to account for replacement of kyanite by symplectites in high pressure granulites. *J. Metamorph. Geol.* 33, 311–330.
- Berger, A., Scherrer, N.C., Bussy, F., 2005. Equilibration and disequilibrium between monazite and garnet: indication from phase-composition and quantitative texture analysis. *J. Metamorph. Geol.* 23, 865–880.
- Bindeman, I.N., Davis, A.M., Drake, M.J., 1998. Ion microprobe study of plagioclase-basalt partition experiments at natural concentration levels of trace elements. *Geochim. Cosmochim. Acta* 62, 1175–1193.
- Breecker, D.O., Sharp, Z.D., 2007. A monazite oxygen isotope thermometer. *Am. Mineral.* 92, 1561–1572.
- Brousseau, A., Stipska, P., Lehmann, J., Schulmann, K., Hacker, B.R., Holder, R., Kylander-Clark, A.R.C., Hanzl, P., Racek, M., Hasalova, P., Lexa, O., Hrdlickova, K., 2015. P–T–D record of crustal-scale thermal flow and magma-assisted doming in the SW Mongolian Altai. *J. Metamorph. Geol.* 33, 359–383.
- Carswell, D.A., Tucker, R.D., O'Brien, P.J., Krogh, T.E., 2003a. Coesite micro-inclusions and the U/Pb age of zircons from the Hareidland eclogite in the Western Gneiss Region of Norway. *Lithos* 67, 181–190.
- Carswell, D.A., Brueckner, H.K., Cuthbert, S.J., Mehta, K., O'Brien, P.J., 2003b. The timing of stabilisation and the exhumation rate for ultra-high pressure rocks in the Western Gneiss Region of Norway. *J. Metamorph. Geol.* 21, 601–612.
- Cesare, B., 2008. Crustal Melting: Working with Enclaves, in *Working with Migmatites*. In: Sawyer, E.W., Brown, M. (Eds.), vol. 38. Mineralogical Association of Canada Short Course Series, pp. 37–55.
- Connolly, J.A.D., Petrin, K., 2002. An automated strategy for calculation of phase diagram sections and retrieval of rock properties as a function of physical conditions. *J. Metamorph. Petrol.* 20 (7), 697–708.
- Corfu, F., Gasser, D., Chew, D.M., 2014. New perspectives on the Caledonides of Scandinavia and related areas: introduction. *Geol. Soc. Lond. Spec. Publ.* 390, 1–8.
- Cuthbert, S.J., Carswell, D.A., Krogh-Ravna, E.J., Wain, A., 2000. Eclogites and eclogites in the Western Gneiss region, Norwegian Caledonides. *Lithos* 52, 165–195.
- Dobrzynetska, L.F., Eide, E.A., Larsson, R.B., Sturt, B.A., Tronnes, R.G., Smith, D.C., Taylor, W.R., Posukhova, T.V., 1995. Microdiamond in high-grade metamorphic rocks of the Western Gneiss Region, Norway. *Geology* 23 (7), 597–600.
- Ewart, A., Griffin, W.L., 1994. Application of proton-microprobe data to trace-element partitioning in volcanic rocks. *Chem. Geol.* 117, 251–284.
- Finger, F., Krenn, E., 2007. Three metamorphic monazite generations in a high-pressure rock from the Bohemian Massif and the potentially important role of apatite in stimulating polyphase monazite growth along a PT loop. *Lithos* 95, 103–115.
- Foster, G., Kinney, P., Vance, D., Prince, C., Harris, N., 2000. The significance of monazite U–Th–Pb age data in metamorphic assemblages; a combined study of monazite and garnet chronometry. *Earth Planet. Sci. Lett.* 181, 327–340.
- Foster, G., Gibson, H.D., Parrish, R., Horstwood, M., Fraser, J., Tindle, A., 2002. Textural, chemical and isotopic insights into the nature and behavior of metamorphic monazite. *Chem. Geol.* 191, 183–207.
- Gordon, S.M., Whitney, D.L., Teysseier, C., Fossen, H., 2013. U–Pb dates and trace-element geochemistry of zircon from migmatite, Western Gneiss Region, Norway: Significance for history of partial melting in continental subduction. *Lithos* 170–171, 35–53. <http://dx.doi.org/10.1016/j.lithos.2013.02.003>.
- Gratz, R., Heinrich, W., 1997. Monazite–xenotime thermobarometry: experimental calibration of the miscibility gap in the binary system CePO₄–YPO₄. *Am. Mineral.* 82, 772–780.
- Hacker, B.R., 2006. Pressures and temperatures of ultrahigh-pressure metamorphism: implications for UHP tectonics and H₂O in subducting slabs. *Int. Geol. Rev.* 48, 1053–1066.
- Hacker, B.R., Gans, P.B., 2005. Continental collisions and the creation of ultrahigh-pressure terranes: petrology and thermochronology of nappes in the central Scandinavian Caledonides. *GSA Bull.* 117, 117–134.
- Hacker, B.R., Andersen, T.B., Johnston, S., Kylander-Clark, A.R.C., Peterman, E.M., Walsh, E.O., Young, D., 2010. High-temperature deformation during continental-margin subduction and exhumation: the ultrahigh-pressure Western Gneiss region of Norway. *Tectonophysics* 480, 149–171.
- Hacker, Bradley R., Kylander-Clark, Andrew R.C., Holder, Robert, Andersen, Torgeir B., Peterman, Emily M., Walsh, Emily O., Munnikhuis, Jonathan K., 2015. Monazite response to ultrahigh-pressure subduction from U–Pb dating by laser ablation split stream. *Chem. Geol.* 409, 28–41.
- Heinrich, W., Andrehs, G., Franz, G., 1997. Monazite–xenotime miscibility gap thermometry: an empirical calibration. *J. Metamorph. Geol.* 15, 3–16.
- Holland, T., Powell, R., 2011. An improved and extended internally consistent thermodynamic dataset for phases of petrological interest, involving a new equation of state for solids. *J. Metamorph. Geol.* 29, 333–383.
- Janots, E., Berger, A., Gnos, E., Whitehouse, M., Lewin, E., Pettke, T., 2012. Constraints on fluid evolution during metamorphism from U–Th–Pb systematic in Alpine hydrothermal monazite. *Chem. Geol.* 326–327, 61–71.
- Jochum, K.P., Stoll, B., Herwig, K., Willbold, M., Hofman, A.W., Amini, M., Aaburg, S., Abouchami, W., Hellebrand, E., Mocek, B., Raczek, I., Stracke, A., Alard, O., Bouman, C., Becker, S., Dücking, M., Bratz, H., Klemd, R., de Bruin, D., Canil, D., Cornell, D., de Hoog, C.-J., Dalpe, C., Danyushevsky, L., Eisenhauer, A., Gao, Y., Snow, J.E., Groschopf, N., Gunther, D., Latkoczy, C., Guillong, M., Hauri, E.H., Hofer, H.E., Lahaye, Y., Horz, K., Jacob, D.E., Kasemann, S.A., Kent, A.J.R., Ludwig, T., Zack, T., Mason, P.R.D., Meixner, A., Rosner, M., Misawa, K., Nash, B.P., Pfander, J., Premo, W.R., Sun, W.D., Tjepolo, M., Vannucci, R., Vennemann, T., Wayne, D., Woodhead, J.D., 2006. MPI-DING reference glasses for in situ microanalysis: new reference values for element concentrations and isotopic ratios. *Geochem. Geophys. Geosyst.* 7 (2), Q02008.
- Jochum, K.P., Weis, U., Stoll, B., Kuzmin, D., Yang, Q., Raczek, I., Jacob, D.E., Stracke, A., Birbaum, K., Frick, D.A., Günther, D., Enzweilerm, J., 2011. Determination of reference values for NISTSRM 610–617 glasses following ISO guidelines. *Geostand. Geoanal. Res.* 35 (4), 397–429.
- Krenn, E., Finger, F., 2010. Unusually Y-rich monazite–(Ce) with 6–14 wt.% Y₂O₃ in granulite from the Bohemian Massif: implications for high-temperature monazite growth from the monazite–xenotime miscibility gap thermometry. *Mineral. Mag.* 74 (2), 217–225.
- Krogh, T.E., Kamo, S.L., Robinson, R., Terry, M.P., Kwok, K., 2011. U–Pb zircon geochronology of eclogites from the Scandian Orogen, northern Western Gneiss Region, Norway: 14–20 million years between eclogite crystallization and return to amphibolite-facies conditions. *Can. J. Earth Sci.* 48 (2), 441–472.
- Kylander-Clark, A.R.C., Hacker, B.R., Johnson, C.M., Beard, B.L., Mahlen, N.J., Lapen, T.J., 2007. Coupled Lu–Hf and Sm–Nd geochronology constrains prograde and exhumation histories of high- and ultrahigh-pressure eclogites from western Norway. *Chem. Geol.* 242 (1–2), 137–154.
- Kylander-Clark, A.R.C., Hacker, B.R., Johnson, C.M., 2009. Slow subduction of a thick ultrahigh-pressure terrane. *Tectonics* 28, TC2003.
- Kylander-Clark, A.R.C., Hacker, B.R., Cottle, J.M., 2013. Laser-ablation split-stream ICP petrochronology. *Chem. Geol.* 345, 99–112.
- Kylander-Clark, A.R.C., Hacker, B.R., 2014. Age and Significance of felsic dikes from the UHP western gneiss region. *Tectonics* 33. <http://dx.doi.org/10.1002/2014TC003582>.
- Ludwig, K.R., 2008. User's Manual for Isoplot 3.6: A Geochronological Toolkit for Microsoft Excel. 4. Berkeley Geochronology Center Special Publication.
- McDonough, W.F., Sun, S.-S., 1995. The composition of the Earth. *Chem. Geol.* 120, 223–253.
- McFarlane, C.R.M., Connelly, J.N., Carlson, W.D., 2005. Monazite and xenotime petrogenesis in the contact aureole of the Makhavinekh Lake Pluton, northern Labrador. *Contrib. Mineral. Petrol.* 148, 524–541.
- Mearns, E.W., 1986. Sm–Nd ages for Norwegian garnet peridotite. *Lithos* 19, 269–278. [http://dx.doi.org/10.1016/0024-4937\(86\)90027-7](http://dx.doi.org/10.1016/0024-4937(86)90027-7).
- Möller, C., 1999. Sapphirine in SW Sweden: a record of Sveconorwegian (–Grenvillian) late-orogenic tectonic exhumation. *J. Metamorph. Geol.* 17, 127–141.
- Mottram, C.M., Warren, C.J., Regis, D., Roberts, N.M.W., Harris, N.B.M., Argles, T.W., Parrish, R., 2014. Developing an inverted Barrovian sequence; insights from monazite petrochronology. *Earth Planet. Sci. Lett.* 403, 418–431.
- Mørk, M.B.E., Mearns, E.W., 1986. Sm–Nd isotopic systematics of a gabbro–eclogite transition. *Lithos* 19, 255–267. [http://dx.doi.org/10.1016/0024-4937\(86\)90026-5](http://dx.doi.org/10.1016/0024-4937(86)90026-5).
- Mysen, B.O., Heier, K.S., 1971. A note on the field occurrence of a large eclogite on Hareid, Sunnmøre, western Norway. *Norsk Geologisk Tidsskrift. Supplement* 50 pp. 93–96.
- Nagy, G., Draganits, E., Demyen, A., Panto, G., Arkai, P., 2002. Genesis and transformations of monazite, florencite, and rhabdophane during medium grade metamorphism: examples from the Sopron Hills, Eastern Alps. *Chem. Geol.* 191, 25–46.
- Nakamura, D., Hirajima, T., 2000. Granulite-facies overprinting of ultrahigh-pressure metamorphic rocks, northeastern Sulu region, eastern China. *J. Petrol.* 41, 563–582.
- Palin, R.M., Searle, M.P., Waters, D.J., Parrish, R.R., Roberts, N.M.W., Horstwood, M.S.A., Yeh, M.-W., Chung, S.-L., Anh, T.T., 2013. A geochronological and petrological study of anatectic paragneiss and associated granite dykes from the Day Nui Con Voi metamorphic core complex, North Vietnam: constraints on the timing of metamorphism within the Red River shear zone. *J. Metamorph. Geol.* 31, 359–387.
- Parrish, R.R., 1990. U–Pb dating of monazite and its application to geological problems. *Can. J. Earth Sci.* 27, 1432–1450.
- Paton, C., Hellstrom, J., Paul, B., Woodhead, J., Hergt, J., 2011. Lolite: freeware for the visualization and processing of mass spectrometer data. *J. Anal. At. Spectrom.* 26, 2508–2518.
- Pearce, N.J.G., Perkins, W.T., Westgate, J.A., Gorton, M.P., Jackson, S.E., Neal, C.R., Chenery, S.P., 1997. A compilation of new and published major and trace element data for NIST SRM 610 and NIST SRM 612 glass reference materials. *Geostand. Newsl. J. Geostand. Geoanal.* 21 (1), 115–144.
- Poirasson, F., Chenery, S., Shepherd, T.J., 2000. Electron microprobe and LA-ICP–MS study of monazite hydrothermal alteration: implications for U–Th–Pb geochronology and nuclear ceramics. *Geochim. Cosmochim. Acta* 64 (19), 3283–3297.
- Pyle, J.M., Spear, F.S., Rudnick, R.L., McDonough, W.F., 2001. Monazite–xenotime–garnet equilibrium in metapelites and a new monazite–garnet thermometer. *J. Petrol.* 42, 2083–2107.
- Romer, R.L., Siegesmund, S., 2003. Why allanite may swindle about its true age. *Contrib. Mineral. Petrol.* 146, 297–307.
- Root, D.B., Hacker, B.R., Gans, P.B., Ducea, M.N., Eide, E.A., Mosenfelder, J.L., 2004. Discrete ultrahigh-pressure domains in the Western Gneiss region, Norway: implications for formation and exhumation. *J. Metamorph. Geol.* 23, 45–61.
- Rubatto, D., Chakraborty, S., Dasgupta, S., 2013. Timescales of crustal melting in the Higher Himalayan Crystallines (Sikkim, Eastern Himalaya) inferred from trace element-constrained monazite and zircon chronology. *Contrib. Mineral. Petrol.* 165, 349–372.
- Rubatto, D., Putlitz, B., Gauthiez-Putallaz, L., Crépisson, C., Buick, I.S., Zheng, Y.-F., 2014. Measurement of in-situ oxygen isotope ratios in monazite by SHRIMP ion microprobe: standards, protocols and implications. *Chem. Geol.* 380, 84–96.
- Seydoux-Guillaume, A.-M., Wirth, R., Heinrich, W., Montel, J.-M., 2002. Experimental determination of thorium partitioning between monazite and xenotime using analytical electron microscopy and X-ray diffraction Rietveld analysis. *Eur. J. Mineral.* 14 (5), 869–878.
- Seydoux-Guillaume, A.-M., Montel, J.-M., Bing, B., Bosse, V., de Parseval, P., Paquette, J.-L., Janots, E., Wirth, R., 2012. Low-temperature alteration of monazite: fluid-mediated coupled dissolution–precipitation, irradiation damage, and disturbance of the U–Pb and Th–Pb chronometers. *Chem. Geol.* 330–331, 140–158.
- Spandler, C., Hermann, J., Arculus, R., Mavrogenes, J., 2003. Redistribution of trace elements during prograde metamorphism from lawsonite blueschist to eclogite facies; implications for deep subduction-zone processes. *Contrib. Mineral. Petrol.* 146, 205–222.

- Spencer, K.J., Hacker, B.R., Kylander-Clark, A.R.C., Andersen, T.B., Cottle, J.M., Stearns, M.A., Poletti, J.E., Seward, G.G.E., 2013. Campaign-style titanite U–Pb dating by laser-ablation ICP: implications for crustal flow, phase transformations and titanite closure. *Chem. Geol.* 341, 84–101.
- Stearns, M.A., Hacker, B.R., Ratschbacher, L., Lee, J., Cottle, J.M., Kylander-Clark, A.R.C., 2013. Synchronous Oligocene–Miocene metamorphism of the Pamir and the north Himalaya driven by plate-scale dynamics. *Geology* 41 (10), 1071–1074.
- Suzuki, K., Adachi, M., 1991. Precambrian provenance and Silurian metamorphism of the Tsubonosawa paragneiss in the South Kitakami terrane, Northeast Japan, revealed by the chemical Th–U–total Pb isochron ages of monazite, zircon, and xenotime. *Geochem. J.* 25, 357–376.
- Terry, M.P., Robinson, P., Krogh Ravn, E.J., 2000a. Kyanite eclogite thermobarometry and evidence for thrusting of UHP over HP metamorphic rocks, Nordøyane, Western Gneiss region, Norway. *Am. Mineral.* 85, 1637–1650.
- Terry, M.P., Robinson, P., Hamilton, M.A., Jercinovic, M.J., 2000b. Monazite geochronology of UHP and HP metamorphism, deformation, and exhumation, Nordøyane, Western gneiss Region, Norway. *Am. Mineral.* 85, 1651–1664.
- Tucker, R.D., Krogh, T.E., Råheim, A., 1990. Proterozoic evolution and age-province boundaries in the central part of the Western Gneiss region, Norway: results of U–Pb dating of accessory minerals from Trondheimsfjord to Geiranger, in Mid-Proterozoic Laurentia–Baltica. In: Gower, C.F., Rivers, T., Ryan, B. (Eds.), *GAC Special Paper*. vol. 38. Geological Association of Canada, St. John's (Newfoundland), pp. 149–173.
- Vaggelli, G., Borghi, A., Cossio, R., Fedi, M., Giuntini, L., Lombardo, B., Marino, A., Massi, M., Olmi, F., Petrelli, M., 2006. Micro-PIXE analysis of monazite from the Dora Maira Massif, Western Italian Alps. *Microchim. Acta* 155, 305–311.
- Vrijmoed, J.C., Austrheim, H., John, T., Hin, R.C., Corfu, F., Davies, G.R., 2013. Metasomatism in the Ultrahigh-pressure Svartberget Garnet–peridotite (Western Gneiss Region, Norway): Implications for the Transport of Crust-derived Fluids within the Mantle. *J. Petrol.* 54, 1815–1848. <http://dx.doi.org/10.1093/ptrology/egt032>.
- Walsh, E.O., Hacker, B.R., 2004. The fate of subducted continental margins: two-stage exhumation of the high-pressure to ultrahigh-pressure Western Gneiss region, Norway. *J. Metamorph. Geol.* 22, 671–687.
- Walsh, E.O., Hacker, B.R., Andersen, T.B., Kylander-Clark, A.R.C., Johnston, S., Peterman, E., Young, D., 2013. Late exhumation of the ultrahigh-pressure Western Gneiss Region: structural geology and structural petrology. *Tectonophysics* 608, 1159–1179.
- Wilke, M., Behrens, H., 1999. The dependence of the partitioning of iron and europium between plagioclase and hydrous tonalitic melt on oxygen fugacity. *Contrib. Mineral. Petrol.* 137, 102–114.
- Young, D.J., Hacker, B.R., Andersen, T.B., Corfu, F., Gehrels, G.E., Grove, M., 2007. Amphibolite to ultrahigh-pressure transition in western Norway: implications for exhumation tectonics. *Tectonics* 26, TC1007.
- Zhu, X.K., O'Nions, R.K., 1999. Monazite chemical composition: some implications for monazite geochronology. *Contrib. Mineral. Petrol.* 137, 351–363.